Influence of the dynamical image potential on the rainbows in ion channeling through short carbon nanotubes

D. Borka,[1] S. Petrović,[1] N. Nešković,[1] D. J. Mowbray,[2] and Z. L. Mišković[2]
[1]*Laboratory of Physics (010), Vinča Institute of Nuclear Sciences, P.O. Box 522, 11001 Belgrade, Serbia and Montenegro*
[2]*Department of Applied Mathematics, University of Waterloo, Waterloo, Ontario, Canada N2L 3G1*
(Received 11 April 2006; published 29 June 2006)

We investigate the influence of the dynamic polarization of the carbon valence electrons on the angular distributions of protons channeled through short (11,9) single-wall carbon nanotubes at speeds of 3 and 5 a.u. (corresponding to the proton energies of 0.223 and 0.621 MeV), with the nanotube length varied from 0.1 to 0.3 μm. The dynamic image force on protons is calculated by means of a two-dimensional hydrodynamic model for the nanotube's dielectric response, whereas the repulsive interaction with the nanotube's cylindrical wall is modeled by a continuum potential based on the Doyle-Turner interatomic potential. The angular distributions of channeled protons are generated by a computer simulation method using the numerical solution of the proton equations of motion in the transverse plane. Our analysis shows that the inclusion of the image interaction causes qualitative changes in the proton deflection function, giving rise to a number of rainbow maxima in the corresponding angular distribution. We propose that observations of those rainbow maxima could be used to deduce detailed information on the relevant interaction potentials, and consequently to probe the electron distribution inside carbon nanotubes.

DOI: 10.1103/PhysRevA.73.062902 PACS number(s): 61.85.+p, 41.75.Ht, 61.82.Rx

I. INTRODUCTION

It is well known that the rainbow effect occurs when sunlight scatters off water droplets [1,2]. It has been demonstrated that the rainbow effect also occurs, and plays important roles in nucleus-nucleus collisions [3–5], atom or ion collisions with atoms or molecules [6], electron-molecule collisions [7], atom or electron scattering from crystal surfaces [8,9], and ion channeling through crystals [10–12].

Quite recently, the rainbow effect has been studied in grazing scattering of keV atoms from metal surfaces under axial surface channeling conditions [13]. It was shown in those studies that well defined peaks in the angular distributions of scattered atoms permit an analysis of the data in terms of scattering potentials. Precise measurements of the rainbow angles in the distributions of scattered atoms enabled the authors [13] to deduce very detailed information on the interatomic potentials at metal surfaces.

The prospect of achieving efficient particle channeling through carbon nanotubes has attracted considerable theoretical interest in the past few years [14–19]. For example, the theory of crystal rainbows, which was formulated as the proper theory of ion channeling in thin crystals [12], has been recently applied to ion channeling through short ropes of achiral carbon nanotubes [17–19], where it has been shown that all the pronounced maxima of the angular distributions of channeled ions, except the maxima lying at the origin, can be attributed to the rainbow effect.

However, relatively little attention has been paid in the reported simulations of ion channeling through carbon nanotubes [14–19] to the effects of dynamic polarization of the carbon valence electrons giving rise to both the ion stopping and the image force which attracts the channeled ion to the nanotube wall [20]. Namely, unlike crystal channels, relatively large "empty" spaces inside carbon nanotubes provide conditions similar to those in ion-surface grazing scattering, where the dynamical image force plays an important role in deflection of ion trajectories [21]. This force has been recently studied for cylindrical channels in solids [22], where it was shown to affect the angular distributions of highly charged ions transmitted through such channels [23]. The importance of the image force has been recently demonstrated in a simulation of ion channeling through a single-wall carbon nanotube [24], where significant spatial redistribution of the ion flux has been predicted after several oscillations of ion trajectories between the nanotube walls.

Given the sensitivity of the rainbow effect to the details of the interaction potential between the incident ion and the nanotube wall, it seems relevant to explore the effects of the image force on the angular distributions of ions channeled through a nanotube. In analogy to ion-surface grazing scattering under axial surface channeling conditions [13], we expect that observations of the rainbow angles in the distributions of channeled ions would enable measurements of details of the interatomic potentials in the nanotube. This information would further facilitate access to studying the electron density distributions inside carbon nanotubes, which are expected to be quite nonhomogeneous, in contrast to the distributions in crystal channels [25].

Consequently, we study in this work the influence of the dynamical polarization effect on the angular distributions of protons channeled through an (11,9) single-wall carbon nanotube, in the energy range between 0.223 and 0.621 MeV, and with a nanotube length varied between 0.1 and 0.3 μm. After outlining the basic theoretical model in Sec. II, we discuss the results of numerical integration of ion trajectories in Sec. III, which is followed by the concluding section. Atomic units are used throughout unless indicated otherwise.

II. THEORY

The system under investigation is a proton moving through an (11,9) single-wall carbon nanotube. The z axis of

our Cartesian coordinate system coincides with the nanotube axis, whereas the xy plane lies at the entrance to the open-ended nanotube. The initial proton velocity vector $\mathbf{v}$ is taken to be parallel to the z axis. For particle channeling through a chiral nanotube, such as (11,9), it is consistent to use the continuum approximation for the elastic interaction potential with carbon atoms on the nanotube wall [26], as well as a jelliumlike model for their valence electrons, both obtained by averaging along the axis and over the circumference of a cylinder of radius R and length L, representing the nanotube. Moreover, if the ion is efficiently steered by the repulsive atomic potential away from the regions of high electron density on the nanotube wall, one can use a two-dimensional (2D) electron gas model for the carbon valence electrons distributed over the surface of the cylinder. In particular, it has been shown that, under such conditions, a 2D hydrodynamic model for the dynamic response of the electron gas provides good approximations for both the ion energy losses due to the collective electron excitations and the dynamical image force [20]. While the ion stopping was found to be relatively week, the image potential on an ion moving paraxially with speed v through the nanotube at distance $r=\sqrt{x^2+y^2}$ from its axis is given by [24]

$$U_{im}(r)=\frac{Z_1^2}{\pi}\sum_{m=-\infty}^{\infty}P\int_0^{\infty}dkI_m^2(kr)K_m^2(kR)\frac{4\pi n_0R(k^2+m^2/R^2)}{(kv)^2-\omega_m^2(k)}, \tag{1}$$

for $0\le r<R$, with

$$\omega_m^2(k)=(k^2+m^2/R^2)[v_s^2+4\pi n_0RI_m(kR)K_m(kR)] \tag{2}$$

being the square of the electron plasma frequency with an angular mode m and longitudinal wave number k, I_m, and K_m the modified Bessel functions, $Z_1=1$ the proton charge, and $v_s\equiv\sqrt{\pi n_0}$ the speed of propagation of the density perturbations in a 2D electron gas with ground-state density n_0 (here, $n_0=0.428$ for carbon nanotubes) [20].

For the repulsive, elastic interaction with the atoms on the nanotube wall, we use the continuum potential based on the Doyle-Turner proton-carbon interaction potential [27] which, after averaging over the azimuthal angle [28], reads

$$U_{\rm at}(r)=\frac{16\pi dZ_1Z_2}{3\sqrt{3}l^2}\sum_{j=1}^{4}a_jb_j^2I_0(b_j^2dr)\exp\{-b_j^2[r^2+(d/2)^2]\}. \tag{3}$$

Here, $Z_2=6$ is the atomic number of carbon, $l=0.144$ nm is the C-C bond length [29], giving the nanotube diameter $d\equiv 2R=1.378$ nm, whereas $a_j=\{3.222,5.270,2.012,0.5499\}\times 10^{-4}$ nm^2 and $b_j=\{10.330,18.694,37.456,106.88\}$ nm^{-1} (corresponding to $a_j=\{0.115,0.188,0.072,0.020\}$ and $b_j=\{0.547,0.989,1.982,5.656\}$ in atomic units) are the fitting parameters [27,28].

In Fig. 1(a) we show the level curves in the range from −2.4 eV to 0 eV with a step of 0.2 eV, for the total potential $U(r)=U_{im}(r)+U_{at}(r)$, defined as a function of proton speed v and radial distance r from the nanotube axis, covering the regions both inside $(0<r<R)$ and outside $(R<r<2R)$ the nanotube of radius $R=13.02$. One can conclude from Fig. 1(a) that the longest ranged effect of the image potential inside the nanotube takes place for $v\approx 5$, whereas the strongest image interaction occurs for $v\approx 3$, giving rise to the deepest potential well which is also the closest to the nanotube wall in comparison to the wells at other speeds. Thus, to emphasize the effects of both the range and the magnitude of the dynamical image force on the rainbow effect, we have chosen to study two proton speeds, $v=3$ and $v=5$.

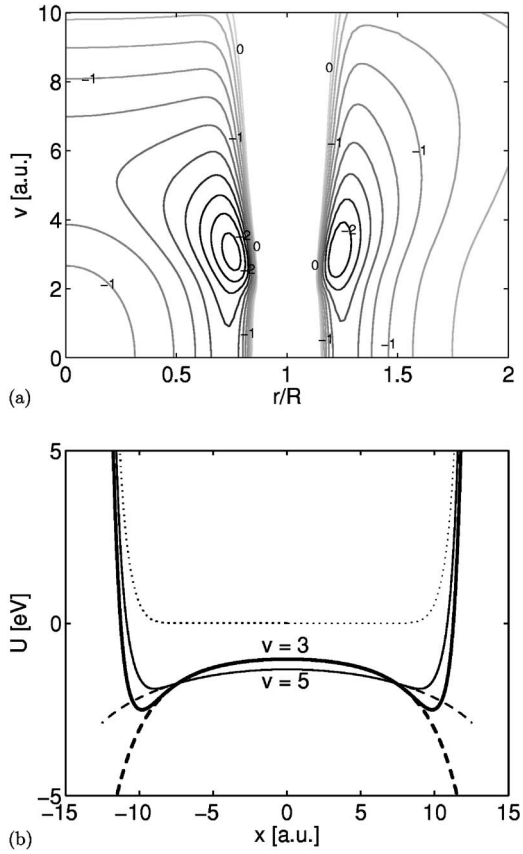

FIG. 1. (a) The level curves of the total potential energy $U(r)=U_{\rm at}(r)+U_{im}(r)$, for a proton moving parallel to the axis of an (11,9) nanotube with radius $R=13.02$ a.u. are shown in the range from −2.4 to 0 eV with a step of 0.2 eV versus the proton speed v (in a.u.) and the reduced radial distance r from the nanotube axis (in units of R), covering the regions both inside $(0<r/R<1)$ and outside $(1<r/R<2)$ the nanotube. (b) Potential energy for transversal motion of a proton along the x axis passing through the center of an (11,9) nanotube, shown on the interval between the nanotube walls, $-R<x<R$ with $R=13.02$ a.u. The dotted curve shows the atomic repulsive potential $U_{\rm at}(|x|)$ from Eq. (3). The thick dashed and solid curves show, respectively, the image potential, $U_{im}(|x|)$ from Eq. (1), and the total potential $U(|x|)$ for a proton speed $v=3$ a.u. The thin dashed and solid curves show, respectively, the image potential, $U_{im}(|x|)$ from Eq. (1), and the total potential $U(|x|)$ for a proton speed $v=5$ a.u.

In our simulations, we neglect all energy losses suffered by the proton, the uncertainty in the proton scattering angle caused by its collisions with the nanotube electrons, as well as the effect of thermal vibrations of the nanotube atoms. The angular distributions of transmitted protons are generated by a Monte Carlo simulation method, in which classical equa-

tions of motion in the transverse directions are solved numerically for a large number of incident protons (3 141 929, to be specific). The x and y components of the proton impact parameter are randomly chosen from a 2D uniform distribution in the entrance plane, such that protons with impact parameters inside the annulus $[R-a,R]$, with $a=[9\pi^2/(128Z_2)]^{1/3}a_0$ being the screening radius and a_0 the Bohr radius, are treated as if they were backscattered and are therefore disregarded. The Cartesian components of the proton scattering angle θ_x and θ_y are obtained from $\theta_x \approx v_x/v_z$ and $\theta_y \approx v_y/v_z$, where v_x and v_y are the transverse and v_z the longitudinal components of the final proton velocity. Under channeling conditions $v_x \ll v_z$ and $v_y \ll v_z$, so that the longitudinal velocity component is practically equal to the initial speed $v_z \approx v$.

As has been recently shown, the angular distributions of channeled protons through short carbon nanotubes can be analyzed by means of the mapping of the impact parameter plane, the xy plane, to the scattering angle plane, the $\theta_x\theta_y$ plane [17–19]. We note that the problem under consideration is essentially one-dimensional owing to the axial symmetry, where the total scattering potential $U(r)=U_{\mathrm{at}}(r)+U_{im}(r)$ is independent of the azimuthal angle. Therefore, any rainbow in our model would show as a sharp circle in the $\theta_x\theta_y$ plane, corresponding to a circle in the impact parameter plane for which the proton differential scattering cross section $\sigma(x,y)$ diverges.

For example, one can consider proton channeling through a very short nanotube, for which the differential scattering cross section σ can be expressed using the impulse approximation as

$$\sigma \approx 1/|J|, \tag{4}$$

where J is the Jacobian of functions $\theta_x(x,y)$ and $\theta_y(x,y)$ [12]. For axially symmetric potentials, one obtains

$$J=\left(\frac{L}{2E}\right)^2 \frac{1}{2r}\frac{d}{dr}F_r^2(r), \tag{5}$$

where L is the nanotube length, E is the incident proton energy, and $F_r(r)=-dU(r)/dr$ is the radial component of the total force. Clearly, one expects a rainbow effect for a very short nanotube whenever $\sigma \to \infty$ due to $J=0$, corresponding to a circle in the impact parameter plane with a radius where the potential $U(r)$ has an inflection point.

It is convenient to take, say, $y=0$ in the impact parameter plane, and use the resulting one-dimensional deflection function $\theta_x(x)$ to analyze the mapping on the $\theta_y=0$ line in the scattering angle plane by studying the extremal points of $\theta_x(x)$ [2]. In Fig. 1(b), we show the total potential $U(|x|)$ along the line $y=0$, in the interval $-R<x<R$ between the opposite walls at the ends of a full nanotube diameter, for two proton speeds, $v=3$ and $v=5$. It is obvious that the inclusion of the image potential gives rise to the inflection points at $x \approx \pm 8.1$ and $x \approx \pm 7.3$ in the functions $U(|x|)$ in Fig. 1(b) for $v=3$ and 5, respectively [compare those values with the positions of extremal points labeled by 1 in the deflection functions shown in Figs. 2(b) and 5(b) for $v=3$ and 5, respectively]. These points would be mapped onto rainbow angles in the distributions of protons over the angles θ_x after channeling through a very short nanotube [similar to the rainbow angles labeled by 1 in Figs. 2(a) and 5(a)].

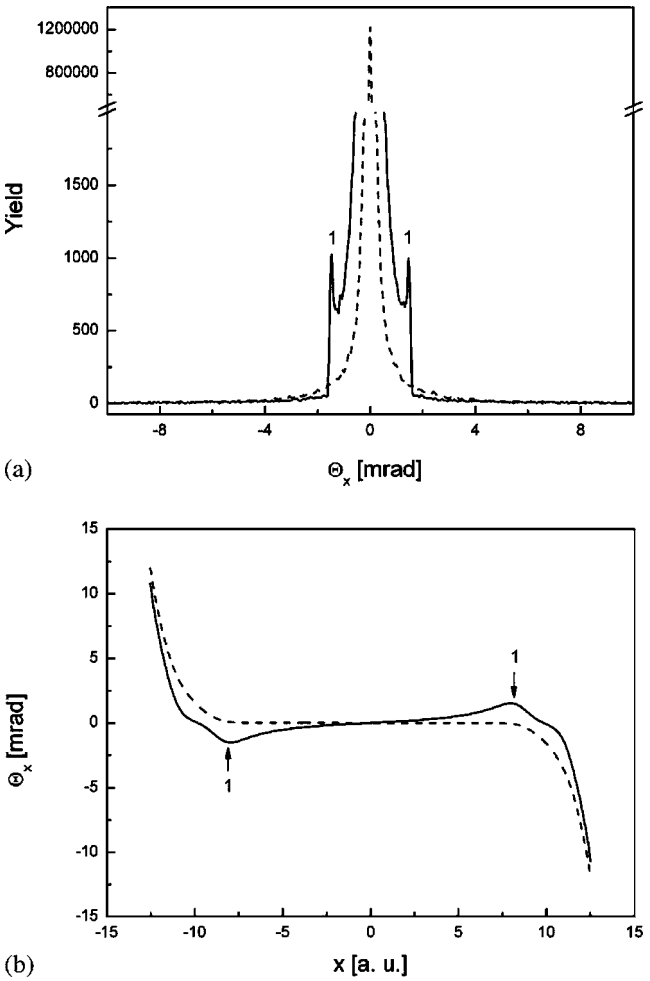

FIG. 2. (a) Angular distributions of channeled protons with the inclusion of the image potential (solid line), and without the inclusion of the image potential (dashed line). (b) The corresponding deflection functions with the inclusion of the image potential (solid line) and without the inclusion of the image potential (dashed line). The proton speed is $v=3$ a.u., corresponding to a proton energy of 0.223 MeV, and the nanotube length is $L=0.1$ μm.

III. RESULTS AND DISCUSSION

Figure 2(a) shows the angular distributions of channeled protons along the θ_x axis for a proton speed of $v=3$ and nanotube length $L=0.1$ μm, in the cases with (solid lines) and without (dashed lines) the dynamical image potential. It is seen that two prominent maxima appear in the angular distribution, located around two scattering angles $\theta_x=\pm 1.5$ mrad, when the image potential is included. Figure 2(b) shows the deflection functions corresponding to the angular distributions shown in Fig. 2(a). One can see that the deflection function without the image interaction has no extremal points, in contrast to the function with the image interaction, which exhibits a pair of symmetrically placed ex-

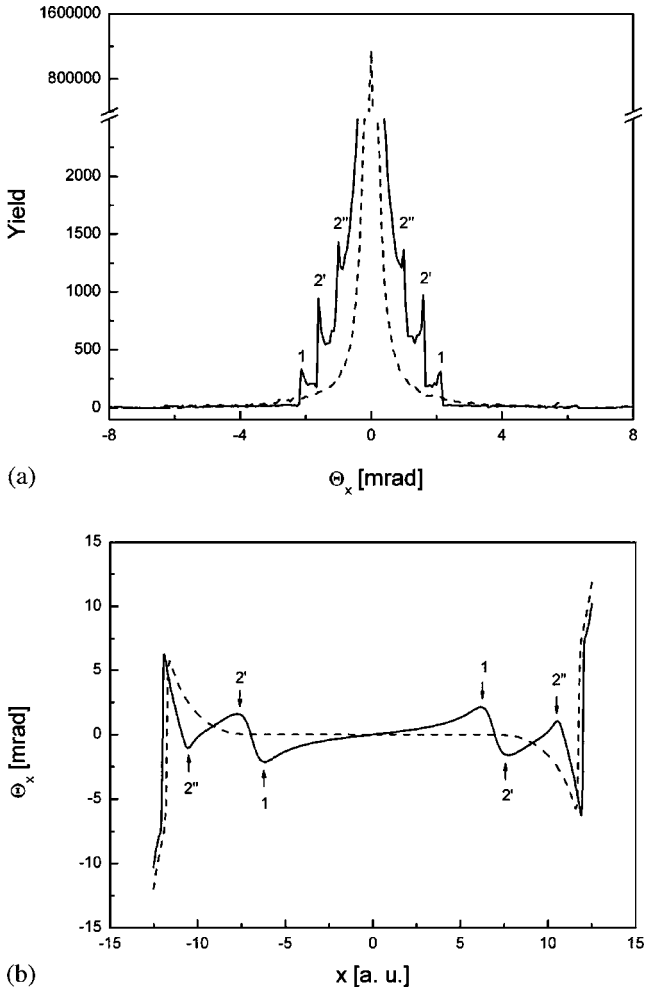

FIG. 3. (a) Angular distributions of channeled protons with the inclusion of the image potential (solid line) and without the inclusion of the image potential (dashed line). (b) The corresponding deflection functions with the inclusion of the image potential (solid line) and without the inclusion of the image potential (dashed line). The proton speed is $v=3$ a.u., corresponding to a proton energy of 0.223 MeV, and the nanotube length is $L=0.2$ μm.

tremal points, labeled by 1. Our analysis shows that the two maxima in the angular distribution in Fig. 2(a), which are also labeled by 1, correspond to the extremal points of the deflection function in Fig. 2(b). Since the extremal points of the deflection function generally define the rainbow angles [2], we conclude that the two prominent maxima of the angular distribution in Fig. 2(a) are the rainbow maxima. It is clear that the rainbow effect occurs as a consequence of the inclusion of the dynamical image potential.

Angular distributions of channeled protons along the θ_x axis for $v=3$ and $L=0.2$ μm, are shown in Fig. 3(a), again for the cases with and without the dynamical image potential. Clearly, six symmetrically placed maxima appear around the angles $\theta_x=\pm 1$, ± 1.6, and ± 2.1 mrad in the distribution with the image interaction included. The corresponding deflection functions are shown in Fig. 3(b). One can see that the deflection function without the image interaction has one pair of extremal points for large values of the impact parameter $|x|$, close to the nanotube wall where the atomic repulsion is significant. The scattering angles corresponding to those extremal points are large and they lie deep in the tails of the corresponding angular distribution in Fig. 3(a), such that no visible structures could be found associated with them. On the other hand, the deflection function in Fig. 3(b) when the image potential is included exhibits three pairs of extremal points, labeled by 1, $2'$, and $2''$, in addition to a pair of extremal points at large $|x|$ values which are close to the pair in the deflection function without the image potential. Our analysis again shows that the six maxima in the angular distribution in Fig. 3(a) correspond to the three pairs of extremal points, labeled by 1, $2'$, and $2''$, in the deflection function, and are, therefore, consequences of the rainbow effect. On the other hand, the large-$|x|$ pair of extremal points in the deflection function with the image potential in Fig. 3(b) occur due to a close approach to the nanotube walls where the repulsive atomic potential dominates over the image potential, and so this pair yields no visible structures in the tails of the corresponding angular distribution in Fig. 3(a).

Figure 4(a) shows the effects of further increasing the nanotube length to $L=0.3$ μm on the angular distributions of channeled protons along the θ_x axis for $v=3$, in the cases with and without the inclusion of the dynamical image potential. One can see that ten maxima appear in the angular distribution with the image potential, which are located around the scattering angles $\theta_x=\pm 0.7$, ± 1.1, ± 1.8, ± 2.1, and ± 2.3 mrad. Figure 4(b) shows the deflection functions corresponding to the angular distributions shown in Fig. 4(a). Similar to Fig. 3, the five pairs of extremal points, labeled by 1, $2'$, $2''$, $3'$, and $3''$, in the deflection function in Fig. 4(b) with the image potential included, correspond to the ten maxima in Fig. 4(a), whereas the two pairs of extremal points of this deflection function at large impact parameters $|x|$ are close to those seen in the deflection function without the image potential. Neither distribution in Fig. 4(a) exhibits visible effects in the scattering angle tails due to those extremal points at large $|x|$ impact parameters, as seen on both curves in Fig. 4(b).

It should be noted that the labeling numbers of the extremal points in Figs. 2(b), 3(b), and 4(b) are in accord with the behavior of the structures in the deflection functions as the nanotube length increases (see Fig. 6). Namely, our analysis shows that, when the nanotube length increases, the extremal points 1 move towards the center of the nanotube ($x=0$), the extremal points $2'$ move in the same direction, while the extremal points $2''$ move outwards. Therefore, the structures associated with the extremal points $3'$ and $3''$ appear in between the extremal points $2'$ and $2''$, when the nanotube length is increased to $L=0.3$ μm.

Finally, we show in Fig. 5(a) the effects of increasing the proton speed to $v=5$ on the angular distributions over the θ_x axis for a nanotube length $L=0.3$ μm, in the cases with and without the inclusion of the dynamical image potential. It is seen that only two pronounced maxima appear in the angular distribution with the image potential, located around the scattering angles $\theta_x=\pm 0.5$ mrad. Figure 5(b) shows the deflection functions corresponding to the angular distributions in Fig. 5(a). One can see that the deflection function without the image potential exhibits a pair of extremal points in the regions of large impact parameters, which give rise to no vis-

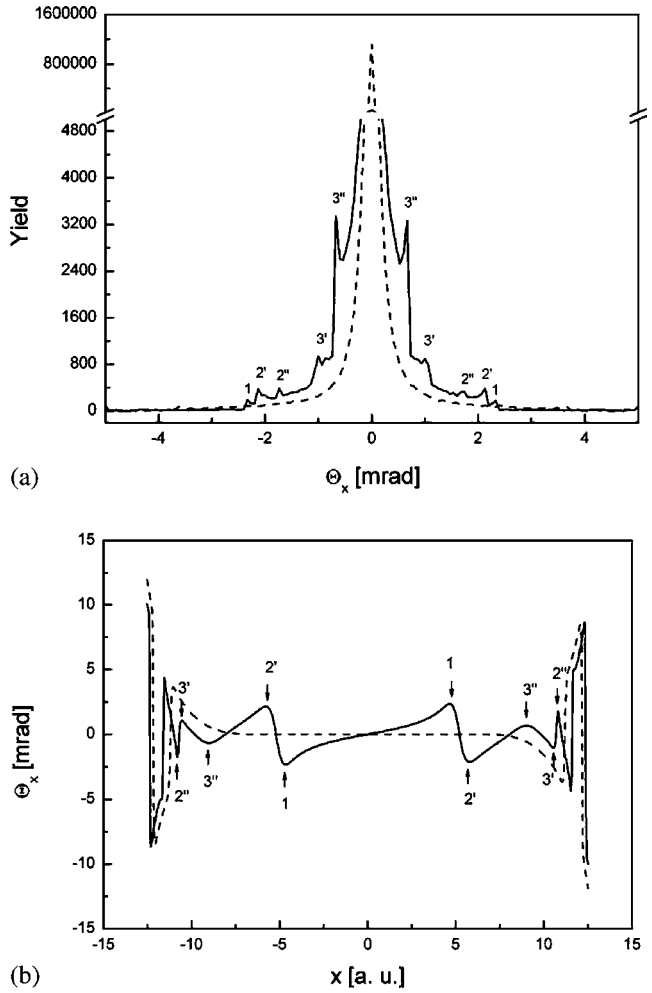

FIG. 4. (a) Angular distributions of channeled protons with the inclusion of the image potential (solid line), and without the inclusion of the image potential (dashed line). (b) The corresponding deflection functions with the inclusion of the image potential (solid line) and without the inclusion of the image potential (dashed line). The proton speed is $v=3$ a.u., corresponding to a proton energy of 0.223 MeV, and the nanotube length is $L=0.3$ μm.

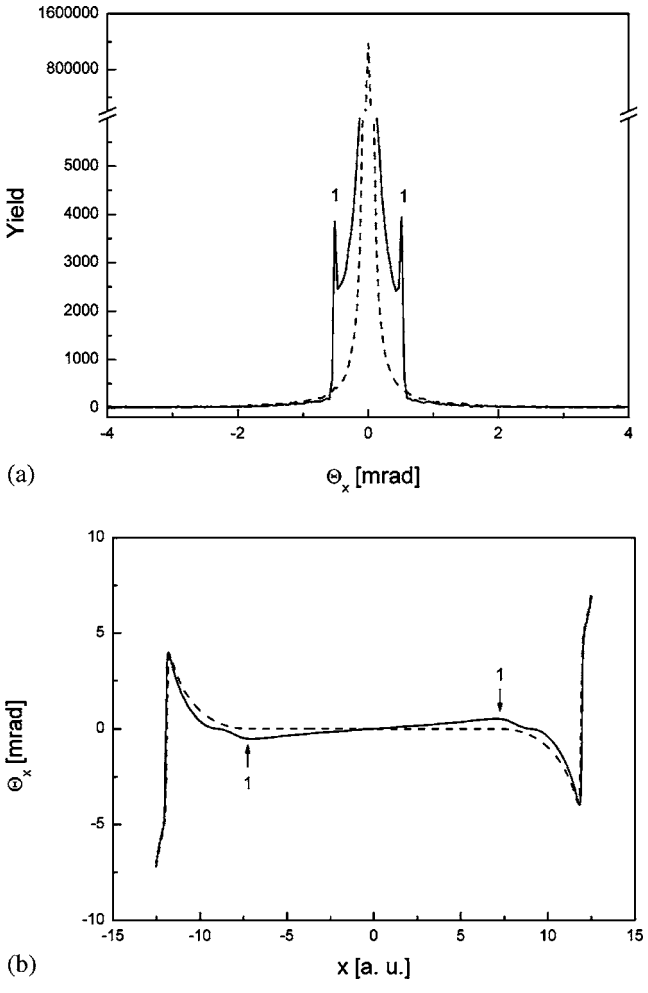

FIG. 5. (a) Angular distributions of channeled protons with the inclusion of the image potential (solid line), and without the inclusion of the image potential (dashed line). (b) The corresponding deflection functions with the inclusion of the image potential (solid line) and without the inclusion of the image potential (dashed line). The proton speed is $v=5$ a.u., corresponding to a proton energy of 0.621 MeV, and the nanotube length is $L=0.3$ μm.

ible structures in the associated angular distribution in Fig. 5(a). The deflection function with the image potential exhibits one pair of extremal points, labeled by 1, and a pair of extremal points close to those in the case without the image potential. While the latter pair again gives no visible structures in the associated angular distribution in Fig. 5(a), our analysis confirms that the two maxima in that distribution do correspond to the extremal points 1 of the deflection function in Fig. 5(b).

Our analysis of the angular distributions of channeled protons at the speed $v=5$ for shorter nanotubes with $L=0.1$ and 0.2 μm revealed hardly visible structures in the angular distributions coming from the inclusion of the image potential. This can be explained by the fact that the magnitude of the dynamical image *force* is much smaller at the speed $v=5$ than at the speed $v=3$ (see Fig. 1). In particular, we note that the extremal points in Fig. 5(b) are close to the inflection points at $x=\pm 7.3$ of the total potential $U(|x|)$, shown in Fig. 1(b) for $v=5$. This suggests that the nanotube length of $L=0.3$ μm can be considered "short" enough to admit the use of the impulse approximation (4) to estimate the rainbow effect at this speed. Moreover, our analysis found no rainbows due to the image interaction for proton speeds $v>5$ for the range of nanotube lengths considered, consistent with the fact that the dynamical image force generally weakens with increasing speed.

The regularity of the appearance of "undulations" in the deflection functions with increasing nanotube length, shown in Figs. 2(b), 3(b), and 4(b), suggests that the oscillations of proton trajectories may be responsible for such regularity. However, it should be borne in mind that oscillations between the nanotube walls do not give rise to visible structures in the angular distributions of channeled protons, but rather the oscillations in the potential well caused by the inclusion of the image interaction are responsible for the onset of the rainbow effect. The latter category of trajectories is related to the impact parameters along the x axis in the interval $-r_c<x<r_c$, where r_c is a solution of the equation

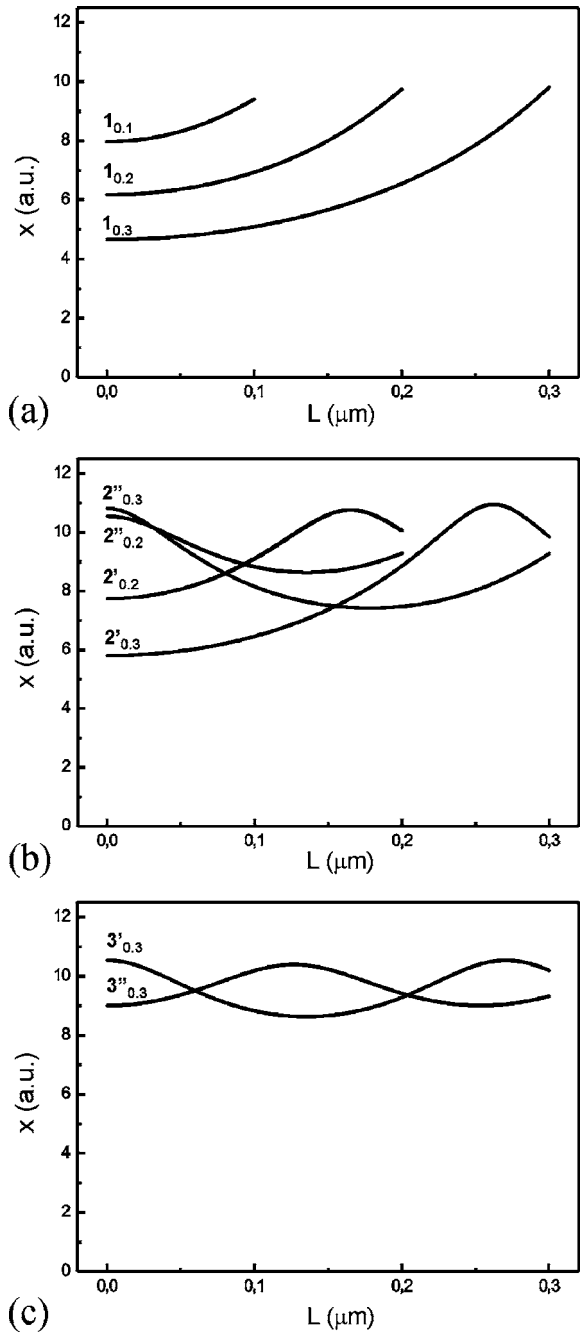

FIG. 6. The rainbow trajectories which experienced (a) one deflection, (b) two deflections, (c) three deflections within the potential wall caused by the dynamic image interaction for proton speed $v=3$ a.u., which is displayed by the thick solid line in Fig. 1(b).

$U(r_c)=U(0)$, giving $r_c = 11.07$ and 10.25 for $v=3$ and 5, respectively [see Fig. 1(b)]. Thus, about 78 and 67 % of all channeled proton trajectories for $v=3$ and 5, respectively, will oscillate within the potential well caused by the image interaction. Among such trajectories, Fig. 6 displays (for $v=3$) those which have impact parameters corresponding to the extremal points in the deflection function and, consequently, exit nanotubes of different lengths at angles close to the rainbow scattering angles. We call such representative trajectories the "rainbow trajectories." Our analysis shows that the rainbow trajectories can be divided into three classes, based on the number of deflections within the potential well caused by the inclusion of the image interaction. The first class, shown in Fig. 6(a), includes the rainbow trajectories that experienced one deflection within the potential well. In this figure, labels $1_{0.1}$, $1_{0.2}$, and $1_{0.3}$ designate the rainbow trajectories for $L=0.1$, 0.2, and 0.3 μm, respectively, which correspond to the extremal points labeled by 1 in the deflection functions in Figs. 2(b), 3(b), and 4(b), as well as to the respective rainbow maxima in Figs. 2(a), 3(a), and 4(a), also labeled by 1. The second class includes the rainbow trajectories that experienced two deflections within the potential well, and they are shown in Fig. 6(b). Here, the rainbow effect can arise only for longer nanotubes with $L=0.2$ and 0.3 μm. There are two types of such trajectories, corresponding to their initial bending away and towards the nanotube axes, which are, respectively, labeled by $2'_{0.2}$ and $2'_{0.3}$ and by $2''_{0.2}$ and $2''_{0.3}$. Thus, the rainbow trajectories $2'_{0.2}$ and $2''_{0.2}$, shown in Fig. 6(b) for $L=0.2$ μm, correspond to the extremal points $2'$ and $2''$ in the deflection function shown in Fig. 3(b), which are associated with the rainbow maxima labeled by $2'$ and $2''$ in Fig. 3(a). Similarly, the rainbow trajectories $2'_{0.3}$ and $2''_{0.3}$, shown in Fig. 6(b) for $L=0.3$ μm, correspond to the extremal points $2'$ and $2''$ in the deflection function in Fig. 4(b), associated with the rainbow maxima $2'$ and $2''$ in Fig. 4(a). The third class of rainbow trajectories, shown in Fig. 6(c), originates from impact parameters close to the potential minimum [see the thick solid curve in Fig. 1(b)] and, because of the weaker forces in that region, such trajectories can give rise to the rainbow effect only in a sufficiently long nanotube ($L=0.3$ μm, in the case shown), after experiencing three deflections within the potential well. Labels $3'_{0.3}$ and $3''_{0.3}$ in Fig. 6(c) designate, respectively, the trajectories which are initially bent towards and away from the nanotube axis, and they correspond to the extremal points $3'$ and $3''$ in the deflection function shown in Fig. 4(b), as well as to the associated rainbow maxima in Fig. 4(a).

Therefore, one can summarize that the extremal points in the deflection functions and the corresponding rainbow maxima in the angular distributions designated by 1, correspond to trajectories which experienced one deflection, those labeled by $2'$ and $2''$ correspond to trajectories which experienced two deflections, and those labeled by $3'$ and $3''$ correspond to trajectories that experienced three deflections within the potential well. It is interesting to note that this situation is partly analogous to the scattering of sunlight off water droplets [1,2], in which the primary, secondary and tertiary rainbows were generated by the rays which experienced one, two, and three reflections within the droplet, respectively. Therefore, we may call the above considered rainbows labeled by 1 the primary rainbows, those labeled by $2'$ and $2''$ the secondary rainbows, and those labeled by $3'$ and $3''$ the tertiary rainbows. In addition, following this partial analogy with the scattering of sunlight off water droplets, we may expect the rainbows of the fourth and higher orders to appear with nanotubes longer than $L=0.3$ μm.

We finally mention that we were not able to detect in our simulations signatures of the zero-degree focusing effect [19], neither in the case without, nor in the case with the dynamical image potential. This is presumably due to our use

of the rather short-ranged Doyle-Turner potential, so that the central potential well in the case without the image potential is much broader than a harmonic well, whereas the image-potential induced potential wells away from the center of the nanotube also exhibit strong anharmonicities.

IV. CONCLUSIONS

We have investigated the influence of the dynamical polarization of electrons in carbon nanotubes on the angular distributions of channeled protons through short (11,9) single-wall carbon nanotubes, in the velocity range from 3 to 5 a.u., corresponding to proton energies from 0.223 to 0.621 MeV, and for nanotube lengths varied from 0.1 to 0.3 μm. It is shown that the dynamic image force on protons gives rise to the extremal points in the deflection function which are otherwise absent when only the elastic repulsive interactions with the carbon atoms on the nanotube walls are considered. As a consequence, well-defined rainbow maxima appear in the angular distributions of channeled protons, which could be measured and used to probe the interatomic interaction potentials in carbon nanotubes. It has been shown that the number of observable rainbow maxima depend on both the proton speed and the length of the nanotube.

We have also shown that the proton trajectories corresponding to the rainbow maxima of the angular distributions can be divided into three classes, depending on the number of deflections within the potential well caused by the image potential. Specifically, we have identified for proton speed $v=3$ a.u. the classes of trajectories which experienced one, two, and three deflections within the potential well. The classes of proton trajectories which have completed increasing numbers of deflections are shown to add new rainbow maxima in the angular distributions as the nanotube length increases.

Apparently, the rather large width of the channels presented by carbon nanotubes reveal the quite important role of the dynamical image interaction in the formation of rainbows during ion channeling through a short nanotube, which is not observed in single-crystal targets. In future work, we plan to extend the scope of this study to double-wall nanotubes, for which the dynamical image potential has already been calculated [30], and to multiwall carbon nanotubes, in which the electrostatic coupling between the nanotube walls gives rise to rich velocity dependences of the dynamical image interactions [31].

ACKNOWLEDGMENTS

D.B., S.P., and N.N. acknowledge support by the Ministry of Science and Environmental Protection of Serbia, and Z.L.M. acknowledges supports by NSERC and PREA.

[1] V. Khare and H. M. Nussenzveig, Phys. Rev. Lett. **33**, 976 (1974); H. M. Nussenzveig, J. Opt. Soc. Am. **69**, 1068 (1979).
[2] J. D. Jackson, Phys. Rep. **320**, 27 (1999).
[3] K. W. Ford and J. A. Wheeler, Ann. Phys. (N.Y.) **7**, 259 (1959).
[4] K. W. McVoy, H. M. Khalil, M. M. Shalaby, and G. R. Satchler, Nucl. Phys. A **455**, 118 (1986).
[5] F. Michel, G. Reidemeister, and S. Ohkubo, Phys. Rev. Lett. **89**, 152701 (2002).
[6] J. N. L. Connor and D. Farrelly, J. Chem. Phys. **75**, 2831 (1981).
[7] G. Ziegler, M. Rädle, O. Pütz, K. Jung, H. Ehrhardt, and K. Bergmann, Phys. Rev. Lett. **58**, 2642 (1987).
[8] A. W. Kleyn and T. C. M. Horn, Phys. Rep. **199**, 191 (1991).
[9] C. O. Reinhold, J. Burgdörfer, K. Kimura, and M. H. Mannami, Phys. Rev. Lett. **73**, 2508 (1994).
[10] N. Nešković, Phys. Rev. B **33**, 6030 (1986).
[11] H. F. Krause, S. Datz, P. F. Dittner, J. Gomez del Campo, P. D. Miller, C. D. Moak, N. Nešković, and P. L. Pepmiller, Phys. Rev. B **33**, 6036 (1986); H. F. Krause, J. H. Barrett, S. Datz, P. F. Dittner, N. L. Jones, J. Gomez del Campo, and C. R. Vane, Phys. Rev. A **49**, 283 (1994).
[12] S. Petrović, L. Miletić, and N. Nešković, Phys. Rev. B **61**, 184 (2000).
[13] A. Schüller, G. Adamov, S. Wethekam, K. Maass, A. Mertens, and H. Winter, Phys. Rev. A **69**, 050901 (2004); A. Schüller, S. Wethekam, A. Mertens, K. Maass, H. Winter, and K. Gärtner, Nucl. Instrum. Methods Phys. Res. B **230**, 172 (2005); H. Winter and A. Schüller, Nucl. Instrum. Methods Phys. Res. B **232**, 165 (2005).
[14] X. Artru, S. P. Fomin, N. F. Shul'ga, K. A. Ispirian, and N. K. Zhevago, Phys. Rep. **412**, 89 (2005).
[15] S. Bellucci, Nucl. Instrum. Methods Phys. Res. B **234**, 57 (2005).
[16] A. V. Krasheninnikov and K. Nordlund, Phys. Rev. B **71**, 245408 (2005).
[17] S. Petrović, D. Borka, and N. Nešković, Eur. Phys. J. B **44**, 41 (2005).
[18] S. Petrović, D. Borka, and N. Nešković, Nucl. Instrum. Methods Phys. Res. B **234**, 78 (2005).
[19] N. Nešković, S. Petrović, and D. Borka, Nucl. Instrum. Methods Phys. Res. B **230**, 106 (2005).
[20] D. J. Mowbray, Z. L. Mišković, F. O. Goodman, and Y.-N. Wang, Phys. Rev. B **70**, 195418 (2004); Phys. Lett. A **329**, 94 (2004).
[21] H. Winter, Phys. Rep. **367**, 387 (2002).
[22] N. R. Arista, Phys. Rev. A **64**, 032901 (2001); N. R. Arista and M. A. Fuentes, Phys. Rev. B **63**, 165401 (2001).
[23] K. Tökési, X. M. Tong, C. Lemell, and J. Burgdörfer, Phys. Rev. A **72**, 022901 (2005).
[24] D.-P. Zhou, Y.-N. Wang, L. Wei, and Z. L. Mišković, Phys. Rev. A **72**, 023202 (2005).
[25] F. E. Leys, C. Amovilli, I. A. Howard, N. H. March, and A. Rubio, J. Phys. Chem. Solids **64**, 1285 (2003).
[26] J. Lindhard, K. Dan. Vidensk. Selsk. Mat. Fys. Medd. **34**, 1 (1965).
[27] P. A. Doyle and P. S. Turner, Acta Crystallogr., Sect. A: Cryst. Phys., Diffr., Theor. Gen. Crystallogr. **24**, 390 (1968).

[28] N. K. Zhevago and V. I. Glebov, Phys. Lett. A **250**, 360 (1998); J. Exp. Theor. Phys. **91**, 504 (2000).

[29] R. Saito, G. Dresselhaus, and M. S. Dresselhaus, *Physical Properties of Carbon Nanotubes* (Imperial College Press, London, 2001).

[30] D. J. Mowbray, S. Chung, Z. L. Mišković, F. O. Goodman, and Y.-N. Wang, Nucl. Instrum. Methods Phys. Res. B **230**, 142 (2005); G. Gumbs, A. Balassis, and P. Fekete, Phys. Rev. B **73**, 075411 (2006).

[31] S. Chung, D. J. Mowbray, Z. L. Mišković, F. O. Goodman, and Y.-N. Wang, Rad. Phys. Chem. (to be published).